

Cite this: *J. Mater. Chem. A*, 2018, 6, 18605

# General and precise carbon confinement of functional nanostructures derived from assembled metal–phenolic networks for enhanced lithium storage†

Zhitong Xiao, Jiashen Meng, Qi Li,\* Xiao Zhang, Ziang Liu, Bo Wen, Chunhua Han and Liqiang Mai \*

Carbon coating strategies have been widely used to enhance the electrochemical performance of electrode materials. However, several issues, including substrate material selectivity, hard control on precise coatings and a limited enhancement of electronic conductivity, hinder the conventional strategies from further practical application. Here, we develop a general, facile and programmable strategy to precisely construct carbon-confined functional nanostructures with high conductivity via metal–phenolic network (MPN) assembly and subsequent controlled pyrolysis. The instantaneous MPN assembly is realized via the coordination reaction between metal ions and phenolic ligands, and the thickness of the MPN shell can be well controlled by simply repeating the rapid assembly procedure. This strategy is further successfully extended to versatile electrode materials with diverse nanostructures and rich compositions. As a proof of concept, the as-synthesized carbon-confined SnO<sub>2</sub> hollow spheres with Fe<sub>2</sub>O<sub>3</sub> nanodots embedded in a carbon shell (SnO<sub>2</sub>@C–Fe<sub>2</sub>O<sub>3</sub>) exhibit a high reversible discharge capacity of 1203 mA h g<sup>-1</sup> after 100 cycles at 0.2 A g<sup>-1</sup>, an excellent cycling stability with a capacity retention of 86% after 1000 cycles at 1 A g<sup>-1</sup>, and a high capacity of 830 mA h g<sup>-1</sup> at a higher rate of 5 A g<sup>-1</sup>. These remarkable performances are attributed to the unique carbon shell, which provides the robust structure to buffer the drastic volume variation and the enhanced electronic conductivity. This programmable and controllable carbon coating strategy opens a new avenue for the design of carbon-incorporated electrode materials for high-performance energy storage.

Received 1st July 2018  
Accepted 29th August 2018

DOI: 10.1039/c8ta06279j

rsc.li/materials-a

## Introduction

With the rapid consumption of fossil energy, lithium-ion batteries (LIBs) have been developed in the direction of high energy density, long lifespan and low cost.<sup>1–4</sup> Graphite, the commercial anode material in LIBs, has a low theoretical specific capacity of only 372 mA h g<sup>-1</sup>, which has become the key bottleneck for further battery breakthroughs.<sup>5–7</sup> Electrode materials like transition metal oxides and sulfides have captured enormous attention as promising candidates for LIB anodes due to their high theoretical specific capacity, environmental friendliness, low cost and abundant resources.<sup>8–10</sup>

State Key Laboratory of Advanced Technology for Materials Synthesis and Processing, International School of Materials Science and Engineering, Wuhan University of Technology, Luoshi Road 122, Wuhan, 430070, Hubei, China. E-mail: qi.li@whut.edu.cn; mlq518@whut.edu.cn

† Electronic supplementary information (ESI) available: Thermogravimetric analysis, morphology characterization, X-ray diffraction, Raman, Brunauer–Emmett–Teller surface area, Fourier transform-infrared, cyclic voltammetry, electrochemical impedance spectroscopy and ampere–voltage curves. See DOI: 10.1039/c8ta06279j

However, the drastic volume variation during the lithiation/delithiation process, their inferior electronic conductivity and the formation of an unstable solid-electrolyte interphase (SEI) layer all lead to a poor rate capacity and inferior cycling stability, which hinder their practical application in fields such as electrical vehicles and portable electronics.<sup>11–13</sup>

To further address the aforementioned issues, several approaches have been adopted. One efficient method is via designing various nanostructures, including nanowires,<sup>14</sup> nanoplates,<sup>15</sup> nanocubes,<sup>16</sup> nanospheres,<sup>17,18</sup> hollow nanostructures,<sup>19–21</sup> and so on, to buffer the volume variation during cycling. However, several issues, including the deformation of the nanostructures during cycling and inferior electronic conductivity, still exist. Another promising approach is to synthesize carbon-confined materials where the conductive carbon shell can endow the inner materials with high electronic conductivity and structure protection, and so result in greatly enhanced cycling and rate performances.<sup>22–25</sup> Extensive research has been devoted to constructing carbon-confined nanostructures through various approaches.<sup>26–32</sup> For example, Huang *et al.*<sup>27</sup> synthesized porous Co/Zn embedded N-doped carbon

nanocages *via* the controlled pyrolysis of the ZIF-8@ZIF-67 precursor. However, a specific metal–organic-framework (MOF) precursor is necessary for this strategy, which limits its broad application. Wang *et al.*<sup>28</sup> developed the synthesis of a  $\text{Li}_4\text{Ti}_5\text{O}_{12}/\text{C}$  composite *via* the sol–gel method, but the thickness of the carbon shell is hard to control. Yang *et al.*<sup>31</sup> reported chestnut-like  $\text{SnO}_2/\text{C}$  nanocomposites with better cycling stability *via* a solution-based synthesis method. However, a low rate performance is obtained, which is due to the limited enhancement of the electronic conductivity associated with the low graphitized carbon coated on  $\text{SnO}_2$ . Therefore, developing a general and facile strategy to rapidly construct precise thickness-controlled carbon-confined nanostructures with high conductivity is of great significance for further practical application.

A metal–phenolic network (MPN) is a supramolecular network structure, which is assembled *via* the coordination bonds between metal ions and phenolic ligands.<sup>33,34</sup> It has been recently used to provide the controllable surface engineering of functional nanomaterials, which show application in drug and gene delivery, catalysis, biosensing and micro-reactors.<sup>35</sup> MPNs recently have attracted much attention in surface engineering because of their special advantages, as follows: (1) the substrates can be various materials, regardless of their composition, size and shape, due to the high binding affinity of phenolic ligands;<sup>33,36</sup> (2) the assembly process is completed instantaneously, which is only one minute for one assembly;<sup>35,37</sup> (3) the thickness of the assembled MPN shell on the substrates can be precisely controlled by simply repeating the rapid assembly;<sup>34,35</sup> (4) the assembly procedure is highly programmable and occurs upon mixing phenolic ligands and metal ions at room temperature with no need for complicated equipment. Besides, the assembled materials are readily available and inexpensive.<sup>33,35</sup> However, to the best of our knowledge, this favorable surface engineering strategy has rarely been applied in the field of electrochemical energy storage.

Herein, we develop a general, facile and programmable strategy to precisely construct  $\text{Fe}_2\text{O}_3$  nanodot-embedded carbon-confined functional nanostructures with high conductivity *via* MPN assembly and subsequent controlled pyrolysis. In brief, the MPN shell was first assembled on the electrode material *via* the coordination reaction between metal ions and phenolic ligands, and then after *in situ* controlled pyrolysis, the  $\text{Fe}_2\text{O}_3$ -embedded carbon shell was obtained. The thickness of the coating shell can be precisely controlled, which was proven *via* a series of characterizations. Moreover, this controllable carbon confinement strategy was applied to diverse electrode nanomaterials with various morphologies and rich compositions. As a proof of concept application, the as synthesized  $\text{Fe}_2\text{O}_3$  nanodot-embedded carbon-confined hollow  $\text{SnO}_2$  spheres ( $\text{SnO}_2@\text{C}-\text{Fe}_2\text{O}_3$ ) exhibited outstanding electrochemical performances when used as an anode material in LIBs, which is due to the robust structure and enhanced electronic conductivity provided by the unique  $\text{Fe}_2\text{O}_3$ -embedded carbon shell.

## Experimental section

### Materials and methods

**Synthesis of  $\text{SnO}_2@\text{C}-\text{Fe}_2\text{O}_3$  hollow spheres.** All the reagents were of analytical grade and used without further purification. In a typical synthesis,  $\text{SnO}_2$  hollow spheres were synthesized *via* a simple hydrothermal method.<sup>38</sup> 0.48 g urea, 0.1 g polyvinylpyrrolidone (PVP, K30,  $M_w = 40\,000$ ) and 0.38 g potassium stannate trihydrate ( $\text{K}_2\text{SnO}_3 \cdot 3\text{H}_2\text{O}$ ) were added to 80 mL of an ethanol–deionized water mixture with 37.5% (v/v) ethanol. After continuous stirring for 10 minutes, the clear solution was then transferred to a 100 mL Teflon-lined stainless steel autoclave. After treatment at 180 °C for 24 h, the autoclave was cooled down to room temperature and then the white product was harvested *via* centrifugation and washed with deionized water and ethanol, before being dried at 70 °C for 12 h. The assembly procedure of the MPN shell was derived from a previous report.<sup>37</sup> In brief, 9.6 mL gallic acid (GA, 15 mM) solution was added to 120 mg of the as-prepared  $\text{SnO}_2$  particles and stirred for 10 s. After that, 4.8 mL iron(III) chloride hexahydrate ( $\text{FeCl}_3 \cdot 6\text{H}_2\text{O}$ , 30 mM) solution was added followed by quick stirring for 3–4 s. Subsequently, the pH of the mixture was adjusted to approximately 4 *via* the addition of 0.48 mL sodium hydroxide (NaOH, 0.5 M) solution followed by stirring for 1 minute. The obtained dark blue product was harvested *via* centrifugation and washing. This process was repeated (1, 3, 7, 10, 15 and 20 times) until MPN shells with a certain number of layers were obtained ( $\text{SnO}_2@\text{MPN}-1$ ,  $\text{SnO}_2@\text{MPN}-3$ ,  $\text{SnO}_2@\text{MPN}-7$ ,  $\text{SnO}_2@\text{MPN}-10$ ,  $\text{SnO}_2@\text{MPN}-15$  and  $\text{SnO}_2@\text{MPN}-20$ ). Finally, after being heated at 500 °C in argon for 2 h, the  $\text{SnO}_2@\text{C}-\text{Fe}_2\text{O}_3-1$ ,  $\text{SnO}_2@\text{C}-\text{Fe}_2\text{O}_3-3$ ,  $\text{SnO}_2@\text{C}-\text{Fe}_2\text{O}_3-7$ ,  $\text{SnO}_2@\text{C}-\text{Fe}_2\text{O}_3-10$ ,  $\text{SnO}_2@\text{C}-\text{Fe}_2\text{O}_3-15$  and  $\text{SnO}_2@\text{C}-\text{Fe}_2\text{O}_3-20$  samples were obtained.

**Synthesis of  $\text{ZnO}@\text{C}-\text{Fe}_2\text{O}_3$  microflowers.**  $\text{ZnO}$  microflowers were prepared using a simple hydrothermal method.<sup>39</sup> 0.35 g zinc acetate dihydrate ( $\text{Zn}(\text{Ac})_2 \cdot 2\text{H}_2\text{O}$ ) was added to 30 mL deionized water and 1.12 g potassium hydroxide (KOH) was added to 5 mL deionized water. The KOH solution was then added dropwise into the  $\text{Zn}(\text{Ac})_2$  solution under continuous stirring for 10 minutes. The clear solution mixture was then transferred into a 50 mL stainless steel autoclave. After treatment at 150 °C for 20 h, the autoclave was cooled down to room temperature and then the white product was collected *via* centrifugation and washed with deionized water and ethanol, before being dried at 70 °C for 12 h. Then, the same assembly procedure that was used for the  $\text{SnO}_2$  particles was applied to the  $\text{ZnO}$  microflowers and this process was repeated twice to obtain  $\text{ZnO}@\text{MPN}$ . Finally, after being heated at 500 °C in argon for 2 h, the  $\text{ZnO}@\text{C}-\text{Fe}_2\text{O}_3$  sample was obtained.

**Synthesis of  $\text{LLO}@\text{C}-\text{Fe}_2\text{O}_3$  nanoparticles.**  $\text{Li}_{1.2}\text{Mn}_{0.54}\text{Ni}_{0.13}\text{Co}_{0.13}\text{O}_2$  nanoparticles were prepared using a sol–gel method according to our recent work.<sup>40</sup> 2.5 g PVP (K30,  $M_w = 40\,000$ ) was first dissolved in 20 mL ethanol. 12.6 mmol lithium acetate dihydrate ( $\text{LiCH}_3\text{COO} \cdot 2\text{H}_2\text{O}$ , Li 5% excess), 5.4 mmol manganese acetate tetrahydrate ( $\text{Mn}(\text{CH}_3\text{COO})_2 \cdot 4\text{H}_2\text{O}$ ), 1.3 mmol nickel acetate tetrahydrate ( $\text{Ni}(\text{CH}_3\text{COO})_2 \cdot 4\text{H}_2\text{O}$ ), and 1.3 mmol

cobalt acetate tetrahydrate ( $\text{Co}(\text{CH}_3\text{COO})_2 \cdot 4\text{H}_2\text{O}$ ) were added to the solution with continuous stirring for 12 h. The mixture was heated at 70 °C for 12 h and the LLO black product was obtained by calcining at 900 °C for 10 h in air. Then, the same assembly procedure that was used for the  $\text{SnO}_2$  particles was applied to the LLO particles, except that the assembly was carried out in ethanol and also washed with ethanol to obtain LLO@MPN. Finally, after being heated at 450 °C in argon for 2 h, the LLO@C- $\text{Fe}_2\text{O}_3$  sample was obtained.

**Synthesis of ZnS@C- $\text{Fe}_2\text{O}_3$  hollow spheres.** ZnS hollow spheres were synthesized *via* a simple hydrothermal method.<sup>41</sup> 1.6 mmol  $\text{Zn}(\text{Ac})_2 \cdot 2\text{H}_2\text{O}$  and 40 mmol thiourea were added into 40 mL of deionized water with continuous stirring for 30 minutes. The solution was then transferred to a 50 mL Teflon-lined stainless steel autoclave. After treatment at 140 °C for 24 h, the autoclave was cooled down to room temperature and then the white product was harvested *via* centrifugation and washed with deionized water and ethanol, before being dried at 70 °C for 12 h. Then, the same assembly procedure that was used for the  $\text{SnO}_2$  particles was applied to the ZnS hollow spheres and the process was repeated ten times to obtain ZnS@MPN. Finally, after being heated at 500 °C in argon for 2 h, the ZnS@C- $\text{Fe}_2\text{O}_3$  sample was obtained.

### Structural characterizations

X-ray diffraction (XRD) characterization was conducted using a D8 Discover X-ray diffractometer with a non-monochromated  $\text{Cu K}_\alpha$  X-ray source ( $\lambda = 1.5418 \text{ \AA}$ ). Scanning electron microscopy (SEM) images were collected using a JEOL JSM-7100F at an acceleration voltage of 20 kV. Transmission electron microscopy (TEM), high resolution TEM (HRTEM) and selected area electron diffraction (SAED) images were obtained using a JEM-2100F/Titan G2 60-300 microscope. Elemental mapping was performed using an EDX-GENESIS 60S spectrometer. Fourier transform-infrared (FT-IR) transmittance spectra were recorded with a Nicolet 60-SXB IR spectrometer. Thermogravimetric analysis (TGA) and differential scanning calorimeter (DSC) curves were recorded with a Netzsch STA 449C simultaneous analyzer. Inductively coupled plasma (ICP) tests were performed using a PerkinElmer Optima 4300DV spectrometer. Raman spectra were conducted using a Renishaw INVIA micro-Raman spectroscopy system. The Brunauer-Emmett-Teller (BET) surface area was measured using nitrogen adsorption isotherms collected at 77 K using a Tristar-3020 instrument. Ampere-voltage curves ( $I$ - $V$  curves) were calculated from a Lake shore PPT4 probe station and an Agilent B1500A semiconductor device analyzer. The  $\text{SnO}_2$  and  $\text{SnO}_2$ @C- $\text{Fe}_2\text{O}_3$ -10 powders were crushed to  $2 \times 1 \times 1$  mm sheets.

### Electrochemical measurement

The working electrode slurry was composed of 70 wt% as-synthesized  $\text{SnO}_2$  or  $\text{SnO}_2$ @C- $\text{Fe}_2\text{O}_3$ -10 powder, 20 wt% acetylene black and 10 wt% carboxymethyl cellulose (CMC) binder. After coating onto Cu foil and then drying at 70 °C for 12 h, the electrode film was cut into 0.785  $\text{cm}^2$  (area) round slices, weighing a total of 1.43–1.71 mg. The areal mass loading was

1.82–2.18  $\text{mg cm}^{-2}$ . The electrochemical measurements were carried out using CR2016 coin-type half-cells at room temperature. Lithium metal foil was used as the counter electrode and the separator was Celgard 2400 microporous membrane. 1 M lithium hexafluorophosphate ( $\text{LiPF}_6$ ) in ethylene carbon (EC)-dimethyl carbonate (DMC) (volume ratio 1 : 1) was used as the electrolyte. Galvanostatic charge/discharge measurements were collected with a multichannel battery testing system (LAND CT2001A). Cycling voltammetry (CV) and electrochemical impedance spectroscopy (EIS) were performed with a CHI 600e electrochemical workstation and Autolab PGSTAT 302N.

## Results and discussion

### Programmable synthesis of controlled carbon-confinement on the $\text{SnO}_2$ hollow spheres

The overall fabrication procedure for the  $\text{SnO}_2$ @C- $\text{Fe}_2\text{O}_3$  hollow spheres is schematically displayed in Fig. 1a. The  $\text{SnO}_2$  hollow spheres were first synthesized *via* a simple hydrothermal method. From SEM and TEM images (Fig. 1b and e), the product exhibits hollow spheres with a size in the range 150–300 nm and an  $\text{SnO}_2$  shell thickness of about 50 nm. Then, a certain amount of GA,  $\text{FeCl}_3 \cdot 6\text{H}_2\text{O}$  and NaOH were added to the as-prepared  $\text{SnO}_2$  hollow spheres step-wise, followed by stirring for one minute.<sup>37</sup> The GA molecules were first adsorbed on the surface of the  $\text{SnO}_2$  hollow spheres due to their high binding affinity.<sup>33,36</sup> Subsequently, the metal ions ( $\text{Fe}^{3+}$ ) were cross-linked with the adsorbed GA molecules to form one layer of the MPN assembly on the  $\text{SnO}_2$  spheres. This assembly process was repeated until a certain number of assembled layers were achieved to obtain MPN-confined  $\text{SnO}_2$  hollow spheres ( $\text{SnO}_2$ @MPN) (Fig. 1c). The surface of the spheres became rough as the number of assembled layers increased, suggesting the existence of the MPN shell as the outer layer of  $\text{SnO}_2$ @MPN (Fig. 1f). Eventually, after controlled pyrolysis, the MPN shell was *in situ* converted into an  $\text{Fe}_2\text{O}_3$ -embedded carbon shell to obtain  $\text{SnO}_2$ @C- $\text{Fe}_2\text{O}_3$ . The morphology of the hollow spheres was well maintained (Fig. 1d) with a continuous coating shell covered on the surfaces of the spheres (Fig. 1g). In brief, this strategy comprises the fast assembly of an MPN shell on the substrate materials, and the *in situ* conversion to an  $\text{Fe}_2\text{O}_3$  nanodot-embedded carbon shell *via* a controlled pyrolysis. Due to the high binding affinity of GA, this carbon confinement strategy is expected to be applied to versatile electrode materials with diverse nanostructures and rich compositions.

Fig. 2 shows several characterizations to prove the formation of the MPN shell on the  $\text{SnO}_2$  hollow spheres. On the basis of the FT-IR spectra (Fig. 2a), peaks at 1380  $\text{cm}^{-1}$  and 1100  $\text{cm}^{-1}$ , originating from the phenolic OH stretching and the phenolic C–O stretching, appeared in the  $\text{SnO}_2$ @MPN spectrum,<sup>42</sup> which suggests the existence of the MPN shell in  $\text{SnO}_2$ @MPN. The HRTEM image of  $\text{SnO}_2$ @MPN (Fig. 2b) shows the continuous, uniform and amorphous MPN shell with a thickness of  $\sim 10$  nm assembled on the surface of the  $\text{SnO}_2$  hollow spheres. The EDX mapping images obviously show the uniform distribution of Sn

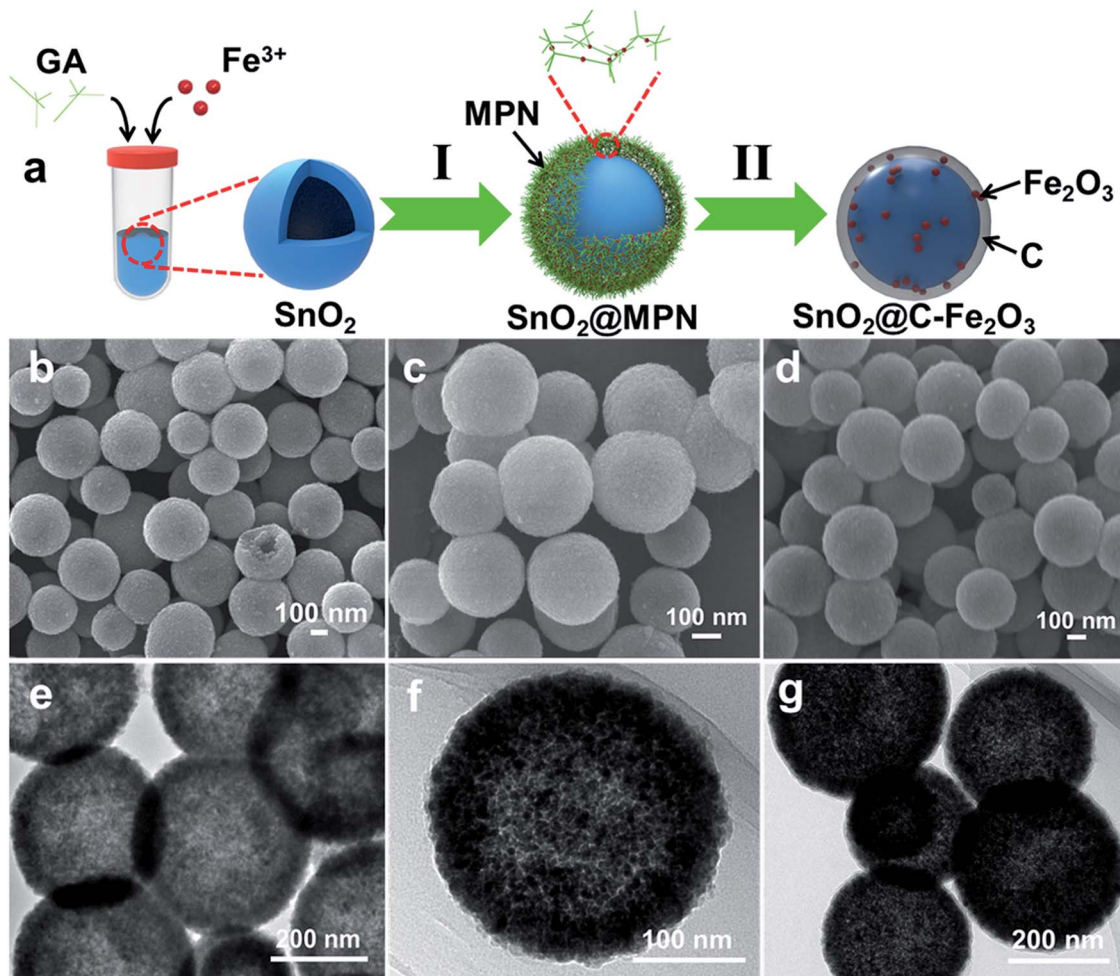


Fig. 1 Synthesis procedure and electron microscopic characterizations of the  $\text{SnO}_2\text{@C-Fe}_2\text{O}_3$  hollow spheres. (a) Schematic illustration of the formation procedure of  $\text{SnO}_2\text{@C-Fe}_2\text{O}_3$ . (b–g) Corresponding SEM and TEM images of  $\text{SnO}_2$  (b & e),  $\text{SnO}_2\text{@MPN}$  (c & f), and  $\text{SnO}_2\text{@C-Fe}_2\text{O}_3$  (d & g).

in the internal  $\text{SnO}_2$  spheres, and C and Fe in the external MPN shell (Fig. 2c).

To prove the assembly of the MPN and the derived carbon shell with controllable shell thickness on the  $\text{SnO}_2$  hollow spheres, a series of characterizations were carried out (Fig. 2). According to the assembly mechanism, the stirring time (20 s or 1 h) has no effect on the shell thickness, implying that the assembly process is completed instantaneously.<sup>35,37</sup> The shell growth is completed when the free  $\text{Fe}^{3+}$  ions in the solution are consumed.<sup>35</sup> Some small aggregates caused by the aggregation of excess  $\text{Fe}^{3+}$ -GA complexes in the solution are bound to the surface of the substrate materials, leading to the increased roughness of the shell as the assembly further proceeds.<sup>35</sup> The thickness of the MPN shell increased as the number of assembly layers increased,<sup>34,35</sup> so the thickness can be well controlled. Here 1, 3, 7, 10, 15 and 20 assembly layers were chosen and the resulted products are denoted as  $\text{SnO}_2\text{@MPN-1}$ ,  $\text{SnO}_2\text{@MPN-3}$ ,  $\text{SnO}_2\text{@MPN-7}$ ,  $\text{SnO}_2\text{@MPN-10}$ ,  $\text{SnO}_2\text{@MPN-15}$  and  $\text{SnO}_2\text{@MPN-20}$ , respectively. From the FT-IR spectra (Fig. 2d), as the assembly proceeded, the typical signal peak at  $1380\text{ cm}^{-1}$ ,

originating from the phenolic OH stretching, gradually got stronger,<sup>42</sup> suggesting that the thickness of the MPN shell increased gradually with the repeated assembly process. On the basis of the TGA results (Fig. S1†), the carbon content values of the derived products  $\text{SnO}_2\text{@C-Fe}_2\text{O}_3\text{-1}$ ,  $\text{SnO}_2\text{@C-Fe}_2\text{O}_3\text{-3}$ ,  $\text{SnO}_2\text{@C-Fe}_2\text{O}_3\text{-7}$ ,  $\text{SnO}_2\text{@C-Fe}_2\text{O}_3\text{-10}$ ,  $\text{SnO}_2\text{@C-Fe}_2\text{O}_3\text{-15}$  and  $\text{SnO}_2\text{@C-Fe}_2\text{O}_3\text{-20}$  are 0.67, 1.54, 3.41, 4.33, 5.79 and 7.51 wt%, respectively. The nearly linear relationship between the carbon content and the number of assembly layers indicates the precise thickness control on the MPN-derived carbon shell coated on the  $\text{SnO}_2$  particles for  $\text{SnO}_2\text{@C-Fe}_2\text{O}_3$  (Fig. 2e). The ICP results of  $\text{SnO}_2\text{@C-Fe}_2\text{O}_3\text{-1}$ ,  $\text{SnO}_2\text{@C-Fe}_2\text{O}_3\text{-3}$ ,  $\text{SnO}_2\text{@C-Fe}_2\text{O}_3\text{-7}$ ,  $\text{SnO}_2\text{@C-Fe}_2\text{O}_3\text{-10}$ ,  $\text{SnO}_2\text{@C-Fe}_2\text{O}_3\text{-15}$  and  $\text{SnO}_2\text{@C-Fe}_2\text{O}_3\text{-20}$  are presented in Table S1.† According to the carbon content results, the deduced content of  $\text{Fe}_2\text{O}_3$  in  $\text{SnO}_2\text{@C-Fe}_2\text{O}_3\text{-1}$ ,  $\text{SnO}_2\text{@C-Fe}_2\text{O}_3\text{-3}$ ,  $\text{SnO}_2\text{@C-Fe}_2\text{O}_3\text{-7}$ ,  $\text{SnO}_2\text{@C-Fe}_2\text{O}_3\text{-10}$ ,  $\text{SnO}_2\text{@C-Fe}_2\text{O}_3\text{-15}$  and  $\text{SnO}_2\text{@C-Fe}_2\text{O}_3\text{-20}$  is 0.61, 1.64, 3.61, 5.28, 7.98 and 12.12 wt%, respectively. The nearly linear relationship between the content of  $\text{Fe}_2\text{O}_3$  and the number of assembly layers also implies the precise thickness control on

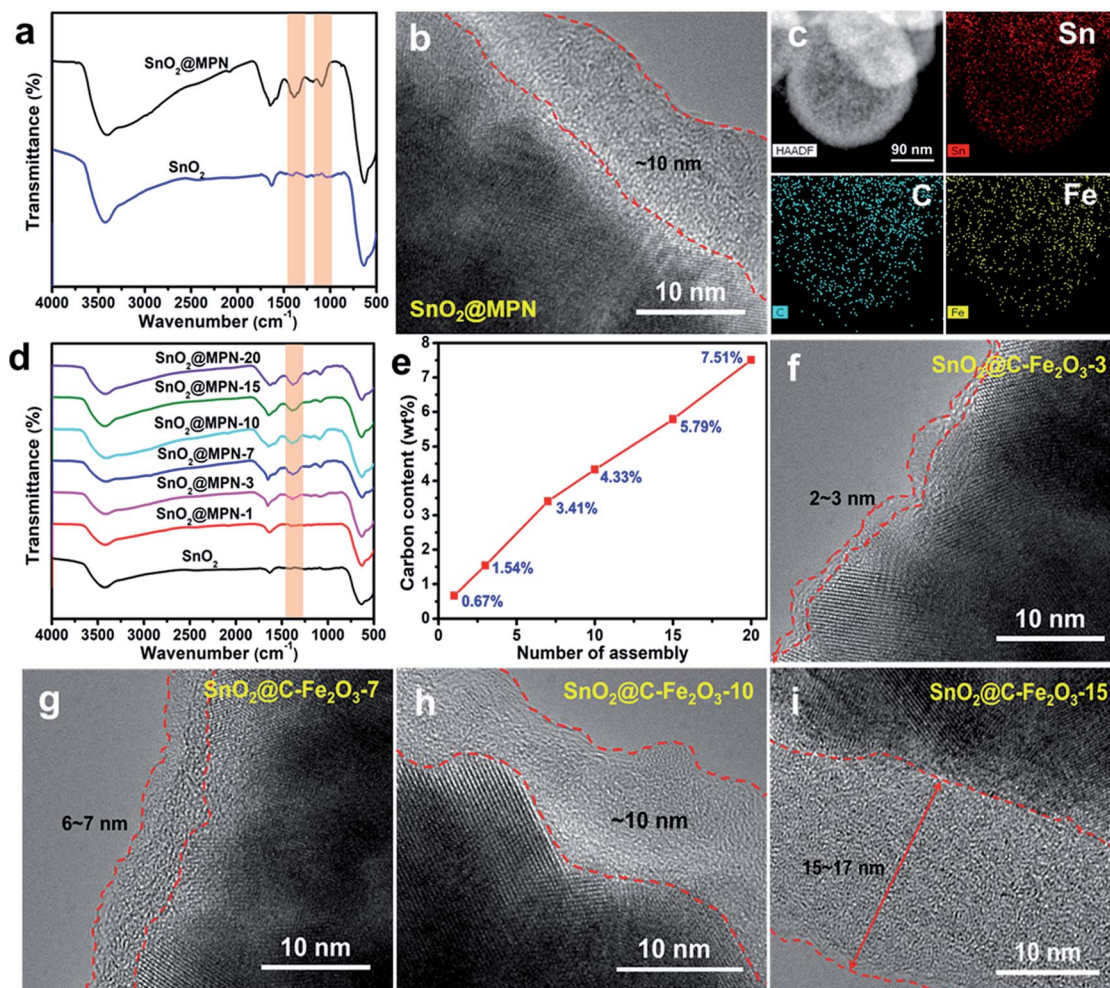


Fig. 2 Characterizations of SnO<sub>2</sub>@MPN and the derived SnO<sub>2</sub>@C-Fe<sub>2</sub>O<sub>3</sub> with a controlled coating thickness. (a) FT-IR spectra of SnO<sub>2</sub> and SnO<sub>2</sub>@MPN. (b) HRTEM image of SnO<sub>2</sub>@MPN. (c) HAADF-STEM image and the corresponding EDX mappings of SnO<sub>2</sub>@MPN for Sn, C and Fe. (d) FT-IR spectra of SnO<sub>2</sub>, SnO<sub>2</sub>@MPN-1, SnO<sub>2</sub>@MPN-3, SnO<sub>2</sub>@MPN-7, SnO<sub>2</sub>@MPN-10, SnO<sub>2</sub>@MPN-15 and SnO<sub>2</sub>@MPN-20. (e) The relationship between the carbon content and the number of assembly layers according to the TGA results. (f-i) HRTEM images of SnO<sub>2</sub>@C-Fe<sub>2</sub>O<sub>3</sub>-3, SnO<sub>2</sub>@C-Fe<sub>2</sub>O<sub>3</sub>-7, SnO<sub>2</sub>@C-Fe<sub>2</sub>O<sub>3</sub>-10 and SnO<sub>2</sub>@C-Fe<sub>2</sub>O<sub>3</sub>-15, respectively.

the MPN-derived carbon shell (Fig. S2†). The HRTEM images (Fig. 2(f-i) and S3†) clearly exhibit the continuous and uniform carbon shell with a thickness of 2-3, 6-7, ~10, 15-17 and 20-22 nm for SnO<sub>2</sub>@C-Fe<sub>2</sub>O<sub>3</sub>-3, SnO<sub>2</sub>@C-Fe<sub>2</sub>O<sub>3</sub>-7, SnO<sub>2</sub>@C-Fe<sub>2</sub>O<sub>3</sub>-10, SnO<sub>2</sub>@C-Fe<sub>2</sub>O<sub>3</sub>-15 and SnO<sub>2</sub>@C-Fe<sub>2</sub>O<sub>3</sub>-20, respectively.

Both the MPN and carbon-confined SnO<sub>2</sub> samples exhibit nearly identical XRD patterns to those of SnO<sub>2</sub> (Fig. S4a and b†), suggesting that the coating procedure has no impact on the crystalline structure of the substrate materials. Two peaks in the Raman spectra (Fig. S4c†) that are located at around 1349 and 1585 cm<sup>-1</sup> are assigned to the D and G bands, respectively.<sup>32,40</sup> The obtained relatively high graphitization nature of the derived carbon coating, which is associated with the superior electronic conductivity of the carbon-confined SnO<sub>2</sub>, might originate from the six-membered benzene ring structure in gallic acid (Fig. S5†). The morphologies of SnO<sub>2</sub>@MPN and SnO<sub>2</sub>@C-Fe<sub>2</sub>O<sub>3</sub> with varied assembly layer numbers are well maintained (Fig. S6a-h†). However, severe aggregation occurs for SnO<sub>2</sub>@MPN-15 and SnO<sub>2</sub>@MPN-20 with the edge of the

particles being blurry and the surface being much rougher (Fig. S6i and k†). Some small aggregates appear on the surfaces of the SnO<sub>2</sub>@C-Fe<sub>2</sub>O<sub>3</sub>-15 and SnO<sub>2</sub>@C-Fe<sub>2</sub>O<sub>3</sub>-20 samples and the hollow sphere morphologies exhibit partial damage (Fig. S6j and l†). Therefore, the 10-times assembly was chosen as the most appropriate to obtain the carbon-confined SnO<sub>2</sub> hollow spheres with a robust carbon shell and a well-preserved structure for investigating the enhanced electrochemical performances.

Fig. 3 shows a series of characterizations to further prove the formation of the C-Fe<sub>2</sub>O<sub>3</sub> shell on the SnO<sub>2</sub> hollow spheres. The XRD pattern (Fig. 3a) shows that all of the reflection peaks can be indexed to the standard PDF card for tetragonal SnO<sub>2</sub> (JCPDS no. 00-041-1445).<sup>6,9,43</sup> The SnO<sub>2</sub>@C-Fe<sub>2</sub>O<sub>3</sub> sample exhibits a nearly identical XRD pattern to that of SnO<sub>2</sub>, indicating that the MPN-derived carbon shell is amorphous. The carbon content of SnO<sub>2</sub>@C-Fe<sub>2</sub>O<sub>3</sub>-10 is 4.33 wt%, which is in agreement with an exothermic peak from the DSC curve (Fig. 3b). The I<sub>D</sub>/I<sub>G</sub> of SnO<sub>2</sub>@C-Fe<sub>2</sub>O<sub>3</sub>-10 was

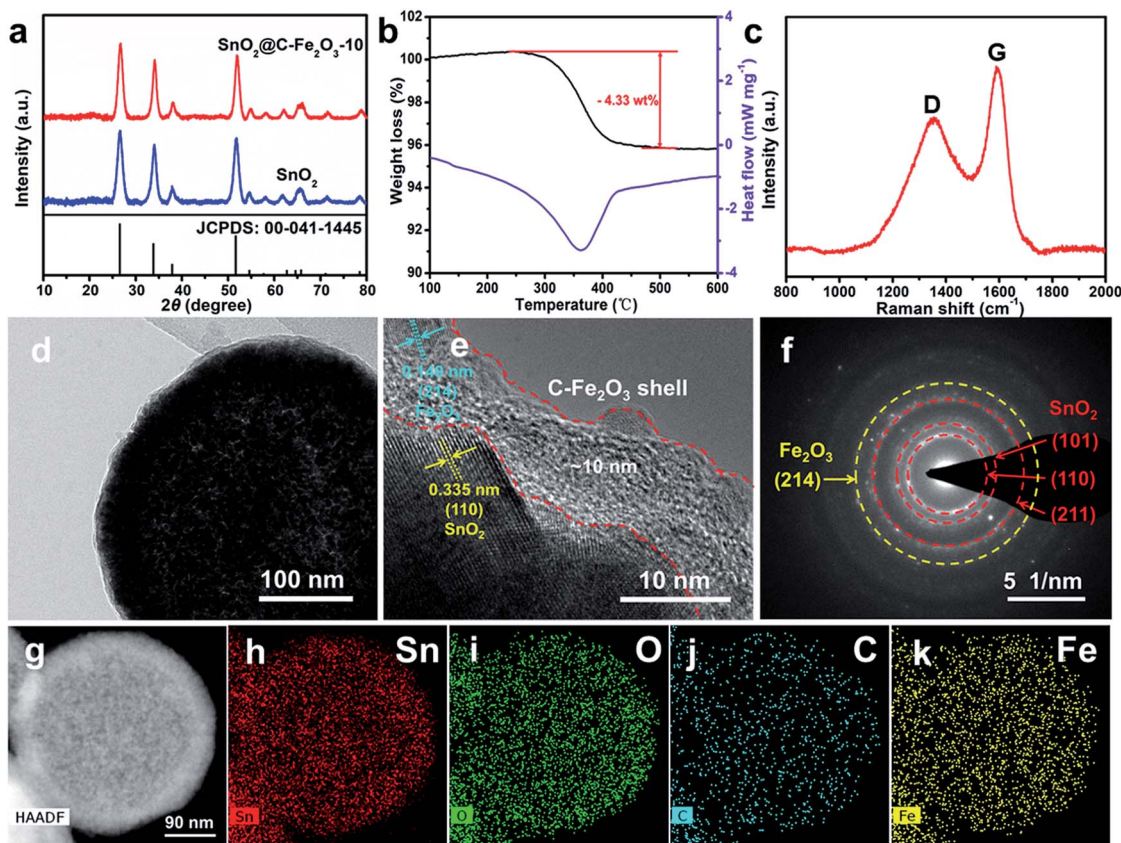


**Fig. 3** Characterizations of  $\text{SnO}_2\text{@C-Fe}_2\text{O}_3\text{-10}$ . (a) XRD patterns of  $\text{SnO}_2$  and  $\text{SnO}_2\text{@C-Fe}_2\text{O}_3\text{-10}$ . (b) TG and DSC curves of  $\text{SnO}_2\text{@C-Fe}_2\text{O}_3\text{-10}$  in air at  $10\text{ }^\circ\text{C min}^{-1}$ . (c) Raman spectrum of  $\text{SnO}_2\text{@C-Fe}_2\text{O}_3\text{-10}$ . (d–f) TEM image, HRTEM image and SAED pattern of  $\text{SnO}_2\text{@C-Fe}_2\text{O}_3\text{-10}$ , respectively. (g–k) HAADF-STEM image and the corresponding EDX mappings of  $\text{SnO}_2\text{@C-Fe}_2\text{O}_3\text{-10}$  for Sn, O, C and Fe.

found to be 0.92, indicating the relatively high graphitization nature of the MPN-derived carbon shell (Fig. 3c). The hollow interior and thin shell of  $\text{SnO}_2\text{@C-Fe}_2\text{O}_3\text{-10}$  are clearly observed in the TEM image (Fig. 3d). The HRTEM image (Fig. 3e) shows that the  $\text{SnO}_2$  hollow spheres are encapsulated underneath a continuous and uniform amorphous carbon layer with a thickness of  $\sim 10\text{ nm}$ . The measured interlayer distance of  $0.335\text{ nm}$  that is observed for the interior spheres is in agreement with the (110) plane of tetragonal  $\text{SnO}_2$ , and the distance of  $0.149\text{ nm}$  that is observed for the outer coating layer is associated with the (214) plane of rhombohedral  $\text{Fe}_2\text{O}_3$ .<sup>44,45</sup> The SAED pattern (Fig. 3f) further verifies the polycrystalline nature of  $\text{SnO}_2\text{@C-Fe}_2\text{O}_3\text{-10}$  and the diffraction rings can be easily assigned to the  $\text{SnO}_2$  phase. Moreover, one diffraction ring is indexed to the (214) plane of the  $\text{Fe}_2\text{O}_3$  phase, further confirming the existence of  $\text{Fe}_2\text{O}_3$ . The EDX mappings confirm the homogeneous distribution of Sn, O, C and Fe (Fig. 3g–k). The nitrogen adsorption–desorption isotherms show that the BET specific surface areas of  $\text{SnO}_2$ ,  $\text{SnO}_2\text{@MPN-10}$  and  $\text{SnO}_2\text{@C-Fe}_2\text{O}_3\text{-10}$  are  $32.73$ ,  $64.91$  and  $53.17\text{ m}^2\text{ g}^{-1}$ , respectively (Fig. S7a–c†). The enhancement of the BET specific surface area after carbon coating can facilitate the ion transport and increase the electrode/electrolyte contact area. The corresponding pore size distributions are presented in Fig. S7d–f.†

### Generality of the carbon confinement strategy

To confirm the generality of our carbon confinement strategy, various electrode materials with diverse nanostructures and rich compositions, including ZnO microflowers, Li-rich layered oxide (LLO) nanoparticles and ZnS hollow spheres, were used for MPN-derived carbon confinement using the aforementioned procedures (Fig. 4). The specific synthesis processes are clearly described in the Experimental section. Initially, the XRD patterns show that the as-synthesized nanostructured electrode materials possess pure phases (Fig. S8a, S9a and S10a†). The SEM and TEM images show the delicate morphologies of the ZnO microflowers, LLO nanoparticles and ZnS hollow spheres in Fig. S8(b & c), S9(b & c) and S10(b & c)†, respectively. Subsequently, certain amounts of GA,  $\text{FeCl}_3\cdot 6\text{H}_2\text{O}$  and NaOH were added to the as-synthesized electrode materials step-wise to generate MPN coatings on the electrode materials. In particular, to testify the universality of this MPN-derived carbon confinement strategy, we also adopted ethanol as the solvent to coat the water-unstable electrode materials such as LLO (Fig. 4e–h). Finally, after controlled pyrolysis, carbon-confined nanostructures were obtained, including  $\text{ZnO@C-Fe}_2\text{O}_3$  microflowers,  $\text{LLO@C-Fe}_2\text{O}_3$  nanoparticles and  $\text{ZnS@C-Fe}_2\text{O}_3$  hollow spheres. The SEM images, elemental mapping images, TEM images, HRTEM images, XRD patterns, FT-IR spectra, TGA

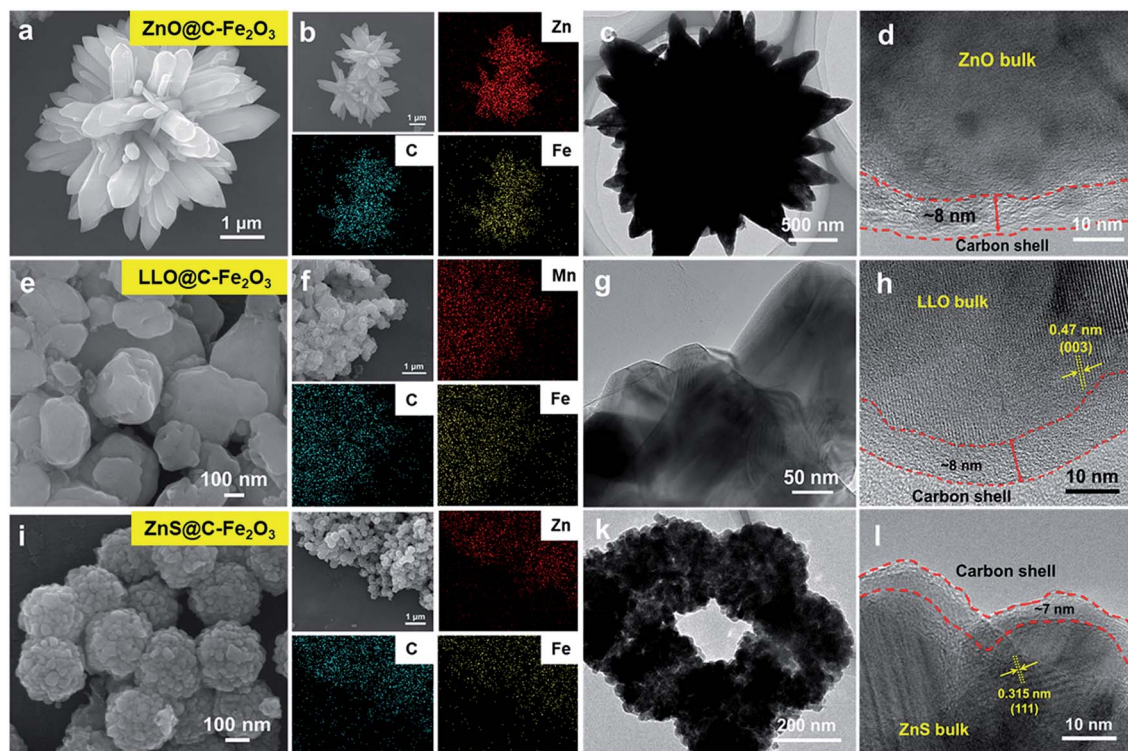


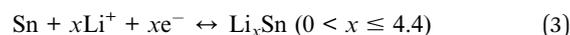
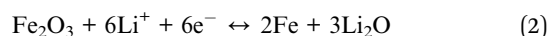
Fig. 4 Generality of the carbon confinement strategy. (a–d) SEM image, elemental mapping images, TEM image and HRTEM image, respectively, of the ZnO@C–Fe<sub>2</sub>O<sub>3</sub> microflowers. (e–h) SEM image, elemental mapping images, TEM image and HRTEM image, respectively, of the LLO@C–Fe<sub>2</sub>O<sub>3</sub> nanoparticles. (i–l) SEM image, elemental mapping images, TEM image and HRTEM image, respectively, of the ZnS@C–Fe<sub>2</sub>O<sub>3</sub> hollow spheres.

curves and Raman spectra (Fig. 4 and S8–S10<sup>†</sup>) give direct evidence of the formation of the coating shell. The delicate morphologies of these architectures can also be well preserved after the coating process with a continuous and uniform carbon shell formed on them. These results indicate that the MPN-derived carbon confinement strategy can be applied to various electrode materials as a result of the high binding affinity of GA,<sup>33,36</sup> regardless of their composition, size and shape, to obtain architecture-preserved precise carbon-confined nanostructures. It is worth noting that the assembly can also easily happen in non-aqueous solvents, which enables the carbon confinement of water-sensitive electrode materials such as LLO. The simple MPN assembly procedure also allows this strategy to be highly programmable, which is favorable for scalable applications. In brief, compared with conventional carbon coating strategies, this MPN-derived carbon confinement method represents a general, facile and programmable strategy to generate a precisely thickness-controlled and high-conductivity carbon coating on various electrode materials with diverse architectures and compositions (Table S2<sup>†</sup>).

### Electrochemical performances

The superior electrochemical performance of SnO<sub>2</sub>@C–Fe<sub>2</sub>O<sub>3</sub>-10 compared to that of SnO<sub>2</sub> was revealed *via* electrochemical characterization in the form of a LIB anode in the potential range 0.01–2.5 V (Fig. 5). The CV curves (Fig. 5a and S11a<sup>†</sup>) of

the first four cycles were measured at 0.2 mV s<sup>-1</sup>. In the first cathodic scan, as shown in Fig. 5a, the reduction peak at 0.88 V can originate from the conversion reactions of SnO<sub>2</sub> and Fe<sub>2</sub>O<sub>3</sub> to Sn and Fe, as described by eqn (1) and (2), respectively, accompanied by the formation of the SEI layers. The clearly discerned peak below 0.25 V can be related to the formation of a Li<sub>x</sub>Sn alloy (eqn (3)). During the subsequent anodic scan, the oxidation peaks at 0.51 V and 1.23 V can be attributed to the dealloying of the Li<sub>x</sub>Sn alloy to Sn and the partially reversible formation of SnO<sub>2</sub>, respectively. The broad peak at about 1.89 V can originate from the reversible oxidation of Fe to Fe<sub>2</sub>O<sub>3</sub>.<sup>44</sup> The obvious difference between the first and subsequent cycles can be interpreted as the formation of SEI layers and the irreversible reaction during the cathodic process. The overlapped curves manifest the high electrochemical reversibility of SnO<sub>2</sub>@C–Fe<sub>2</sub>O<sub>3</sub>-10. The main electrochemical processes can be described as follows:



When tested at 0.2 A g<sup>-1</sup> (Fig. 5b), the first Coulombic efficiency of the SnO<sub>2</sub>@C–Fe<sub>2</sub>O<sub>3</sub>-10 electrode is 76%, which is

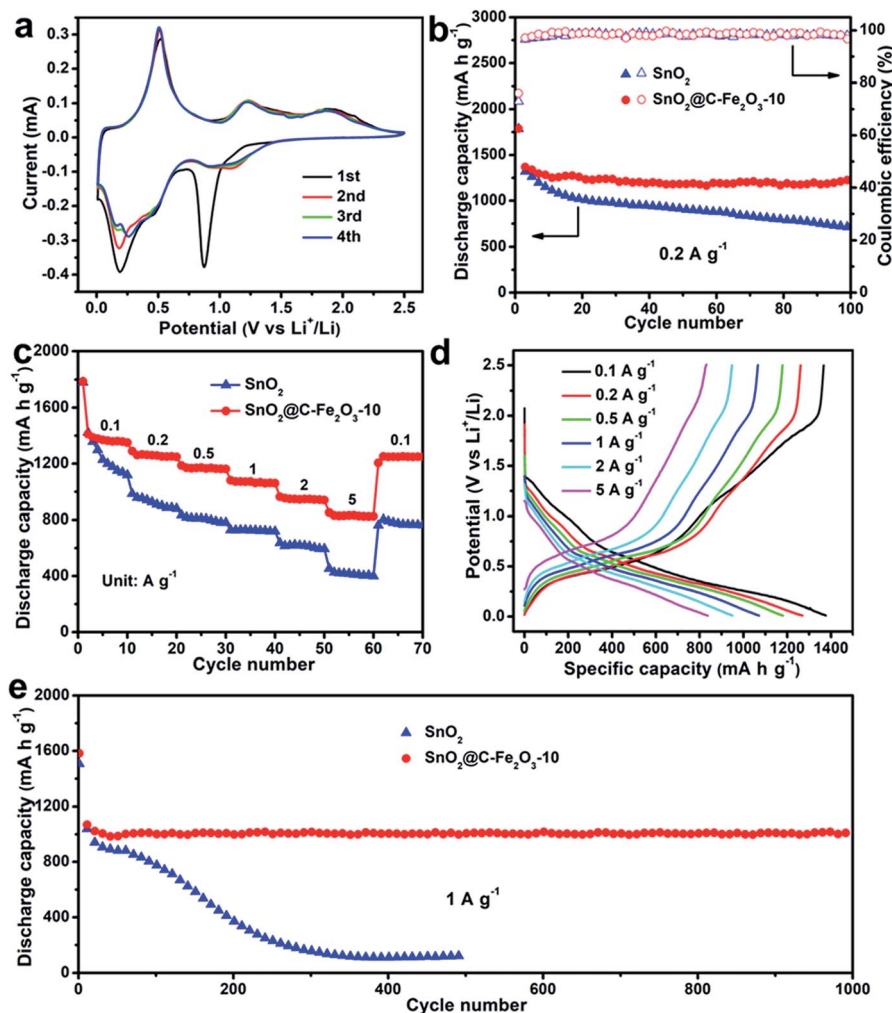


Fig. 5 Electrochemical performances of the SnO<sub>2</sub> and SnO<sub>2</sub>@C-Fe<sub>2</sub>O<sub>3</sub>-10 samples in the potential range 0.01–2.5 V. (a) CV curves of the first four cycles for SnO<sub>2</sub>@C-Fe<sub>2</sub>O<sub>3</sub>-10 at a scan rate of 0.2 mV s<sup>-1</sup>. (b) Cycling performance and the corresponding Coulombic efficiencies tested at a current density of 0.2 A g<sup>-1</sup>. (c) Rate performance conducted at current densities of 0.1, 0.2, 0.5, 1, 2 and 5 A g<sup>-1</sup>. (d) The corresponding charge-discharge voltage profiles of SnO<sub>2</sub>@C-Fe<sub>2</sub>O<sub>3</sub>-10 at different current densities. (e) Long-term cycling performance at a current density of 1 A g<sup>-1</sup>.

higher than that of SnO<sub>2</sub> (72%). After 100 cycles, the SnO<sub>2</sub>@C-Fe<sub>2</sub>O<sub>3</sub>-10 electrode exhibits a high capacity (1203 mA h g<sup>-1</sup>) and a stable cycling performance (a capacity retention of 91%), compared to those of SnO<sub>2</sub> (712 mA h g<sup>-1</sup> and 53%). The average specific discharge capacities of SnO<sub>2</sub>@C-Fe<sub>2</sub>O<sub>3</sub>-10 are 1376, 1264, 1177, 1072, 954 and 830 mA h g<sup>-1</sup> at 0.1, 0.2, 0.5, 1, 2 and 5 A g<sup>-1</sup>, respectively, while the corresponding capacities of SnO<sub>2</sub> are 1206, 933, 818, 725, 624 and 421 mA h g<sup>-1</sup> (Fig. 5c). The capacity quickly recovers to 1250 mA h g<sup>-1</sup> when the current density is reduced back to 0.1 A g<sup>-1</sup>, suggesting the structural stability of SnO<sub>2</sub>@C-Fe<sub>2</sub>O<sub>3</sub>-10. The corresponding charge-discharge voltage profiles of the rate performance (Fig. 5d) exhibit low polarization and a high capacity reversibility of SnO<sub>2</sub>@C-Fe<sub>2</sub>O<sub>3</sub>-10. The long-term cycling performances at 1 A g<sup>-1</sup> are displayed in Fig. 5e. The capacity of the SnO<sub>2</sub> electrode quickly decreases to below 160 mA h g<sup>-1</sup> after 300 cycles. However, the SnO<sub>2</sub>@C-Fe<sub>2</sub>O<sub>3</sub>-10 electrode exhibits fabulous cycling stability, and a high reversible capacity of 1003 mA h g<sup>-1</sup> (a capacity retention of 86%) was obtained after 1000 cycles. The

1st, 2nd, 10th, 50th and 100th cycle charge-discharge voltage profiles of SnO<sub>2</sub> and SnO<sub>2</sub>@C-Fe<sub>2</sub>O<sub>3</sub>-10 at 0.2 A g<sup>-1</sup> and the corresponding charge-discharge voltage profiles of SnO<sub>2</sub> are presented in Fig. S11b-d,† further confirming the enhanced electrochemical performance of SnO<sub>2</sub>@C-Fe<sub>2</sub>O<sub>3</sub>-10. The C-Fe<sub>2</sub>O<sub>3</sub> composite derived from pure MPN with a rhombohedral structure was also studied, and it exhibited high capacities of 1308 mA h g<sup>-1</sup> at 0.2 A g<sup>-1</sup> after 30 cycles and 1112 mA h g<sup>-1</sup> at 1 A g<sup>-1</sup> after 150 cycles (Fig. S12†). Taking into account the C-Fe<sub>2</sub>O<sub>3</sub> wt% in SnO<sub>2</sub>@C-Fe<sub>2</sub>O<sub>3</sub>-10 according to the composition analysis results, the capacity contribution of the C-Fe<sub>2</sub>O<sub>3</sub> shell in SnO<sub>2</sub>@C-Fe<sub>2</sub>O<sub>3</sub>-10 is about 120 mA h g<sup>-1</sup>, corresponding to approximately 10% of the total capacity.

The superior electrochemical performance of SnO<sub>2</sub>@C-Fe<sub>2</sub>O<sub>3</sub>-10 as an anode material for LIBs compared to some previous reports (Table S3†) is attributed to the MPN-derived unique C-Fe<sub>2</sub>O<sub>3</sub> shell. First, the robust protective shell can buffer the drastic volume variation during the lithiation/delithiation process, and thus guarantee the structural

integrity of the hollow spheres. The morphology of SnO<sub>2</sub>@C-Fe<sub>2</sub>O<sub>3</sub>-10 is well-preserved after cycling (Fig. S13b†). However, under the same testing conditions, the morphology of the SnO<sub>2</sub> spheres in the LIB anode is seriously damaged. Second, the relatively high graphitization nature of the continuous carbon shell can enhance the electronic conductivity and ion transport. The EIS plots, which were obtained at 2.5 V after 100 cycles at 0.2 A g<sup>-1</sup> (Fig. S14†), show that the charge-transfer and diffusion resistances of SnO<sub>2</sub>@C-Fe<sub>2</sub>O<sub>3</sub>-10 are smaller than those of SnO<sub>2</sub>, suggesting faster electronic and ion transports. Moreover, the conductivity, according to the *I-V* curves (Fig. S15†) of SnO<sub>2</sub>@C-Fe<sub>2</sub>O<sub>3</sub>-10, is about 20 times higher than that of SnO<sub>2</sub> (Fig. S13†). Third, the embedded Fe<sub>2</sub>O<sub>3</sub> nanodots can contribute to facilitating the reversibility of the electrochemical reaction (eqn (1)) and enhancing the cycling stability owing to the reversible conversion of Fe/Li<sub>2</sub>O into Fe<sub>2</sub>O<sub>3</sub>.<sup>44,46</sup>

## Conclusions

A general, facile and programmable MPN-derived carbon confinement strategy has been developed *via* instantaneous MPN assembly and subsequent controlled pyrolysis. The precisely thickness-controlled carbon confinement has been successfully applied to versatile electrode materials with diverse nanostructures and compositions. As a proof-of-concept application, the obtained carbon-confined SnO<sub>2</sub>@C-Fe<sub>2</sub>O<sub>3</sub>-10 hollow spheres, used as an LIB anode, exhibited superior cycling stability and excellent rate capacity with a retained capacity of 1003 mA h g<sup>-1</sup> after 1000 cycles at 1 A g<sup>-1</sup> and a high reversible capacity of 830 mA h g<sup>-1</sup> at 5 A g<sup>-1</sup>. The enhanced electrochemical performance is mainly attributed to the robust structure and enhanced electronic conductivity provided by the unique Fe<sub>2</sub>O<sub>3</sub>-embedded carbon shell. Our work provides new insight into the synthesis of carbon-incorporated electrode materials for high-performance energy storage.

## Conflicts of interest

There are no conflicts to declare.

## Acknowledgements

This work was supported by the National Natural Science Fund for Distinguished Young Scholars (51425204), the National Natural Science Foundation of China (51521001), the National Key Research and Development Program of China (2016YFA0202603), the Programme of Introducing Talents of Discipline to Universities (B17034), the Yellow Crane Talent (Science & Technology) Program of Wuhan City, the International Science & Technology Cooperation Program of China (2013DFA50840) and the Fundamental Research Funds for the Central Universities (WUT: 2016III001, 2017III009).

## Notes and references

1 L. Mai, M. Yan and Y. Zhao, *Nature*, 2017, **546**, 469–470.

- J. Meng, X. Liu, J. Li, Q. Li, C. Zhao, L. Xu, X. Wang, F. Liu, W. Yang, X. Xu, Z. Liu, C. Niu and L. Mai, *Nano Lett.*, 2017, **17**, 7773–7781.
- X. Wang and G. Yushin, *Energy Environ. Sci.*, 2015, **8**, 1889–1904.
- S. Chu, Y. Cui and N. Liu, *Nat. Mater.*, 2016, **16**, 16–22.
- Y. Tang, Y. Zhang, W. Li, B. Ma and X. Chen, *Chem. Soc. Rev.*, 2015, **44**, 5926–5940.
- K. Lu, Z. Hu, J. Ma, H. Ma, L. Dai and J. Zhang, *Nat. Commun.*, 2017, **8**, 527.
- A. R. Kamali, H.-K. Kim, K.-B. Kim, R. Vasant Kumar and D. J. Fray, *J. Mater. Chem. A*, 2017, **5**, 19126–19135.
- Y. Zhong, M. Yang, X. Zhou and Z. Zhou, *Mater. Horiz.*, 2015, **2**, 553–566.
- K. Lu, Z. Hu, Z. Xiang, J. Ma, B. Song, J. Zhang and H. Ma, *Angew. Chem., Int. Ed.*, 2016, **128**, 10604–10608.
- J. Li, D. Yan, X. Zhang, S. Hou, T. Lu, Y. Yao and L. Pan, *J. Mater. Chem. A*, 2017, **5**, 20428–20438.
- H. Yang, Y. Zhang, F. Hu and Q. Wang, *Nano Lett.*, 2015, **15**, 7616–7620.
- J. Liu, L. Yu, C. Wu, Y. Wen, K. Yin, F. K. Chiang, R. Hu, J. Liu, L. Sun, L. Gu, J. Maier, Y. Yu and M. Zhu, *Nano Lett.*, 2017, **17**, 2034–2042.
- Y. Wang, J. Han, X. Gu, S. Dimitrijević, Y. Hou and S. Zhang, *J. Mater. Chem. A*, 2017, **5**, 18737–18743.
- Y. Dong, S. Li, K. Zhao, C. Han, W. Chen, B. Wang, L. Wang, B. Xu, Q. Wei, L. Zhang, X. Xu and L. Mai, *Energy Environ. Sci.*, 2015, **8**, 1267–1275.
- G. D. Park, J.-K. Lee and Y. C. Kang, *Adv. Funct. Mater.*, 2017, **27**, 1603399.
- F. Zheng, D. Zhu, X. Shi and Q. Chen, *J. Mater. Chem. A*, 2015, **3**, 2815–2824.
- L. Li, J. Deng, R. Yu, J. Chen, Z. Wang and X. Xing, *J. Mater. Chem. A*, 2013, **1**, 11894–11900.
- R. Sun, S. Liu, Q. Wei, J. Sheng, S. Zhu, Q. An and L. Mai, *Small*, 2017, **13**, 1701744.
- H. Wang, J. Wang, S. Xie, W. Liu and C. Niu, *Nanoscale*, 2018, **10**, 6159–6167.
- L. Shen, L. Yu, H. B. Wu, X. Y. Yu, X. Zhang and X. W. Lou, *Nat. Commun.*, 2015, **6**, 6694.
- C. Han, F. Liu, J. Liu, Q. Li, J. Meng, B. Shao, Q. He, X. Wang, Z. Liu and L. Mai, *J. Mater. Chem. A*, 2018, **6**, 6220–6224.
- X. Zhou, L. Yu and X. W. D. Lou, *Adv. Energy Mater.*, 2016, **6**, 1600451.
- B. Huang, X. Li, Y. Pei, S. Li, X. Cao, R. C. Masse and G. Cao, *Small*, 2016, **12**, 1945–1955.
- Y. Zang, H. Zhang, X. Zhang, R. Liu, S. Liu, G. Wang, Y. Zhang and H. Zhao, *Nano Res.*, 2016, **9**, 2123–2137.
- J. Wu, Z. Lu, K. Li, J. Cui, S. Yao, M. Ihsan-ul Haq, B. Li, Q.-H. Yang, F. Kang, F. Ciucci and J.-K. Kim, *J. Mater. Chem. A*, 2018, **6**, 5668–5677.
- F. Xie, L. Zhang, D. Su, M. Jaroniec and S. Z. Qiao, *Adv. Mater.*, 2017, **29**, 1700989.
- M. Huang, K. Mi, J. Zhang, H. Liu, T. Yu, A. Yuan, Q. Kong and S. Xiong, *J. Mater. Chem. A*, 2017, **5**, 266–274.
- J. Wang, X.-M. Liu, H. Yang and X.-d. Shen, *J. Alloys Compd.*, 2011, **509**, 712–718.

- 29 L. Cheng, J. Yan, G.-N. Zhu, J.-Y. Luo, C.-X. Wang and Y.-Y. Xia, *J. Mater. Chem.*, 2010, **20**, 595–602.
- 30 S. Boukhalfa, K. Evanoff and G. Yushin, *Energy Environ. Sci.*, 2012, **5**, 6872–6879.
- 31 L. Yang, T. Dai, Y. Wang, D. Xie, R. L. Narayan, J. Li and X. Ning, *Nano Energy*, 2016, **30**, 885–891.
- 32 Q. He, J. Liu, Z. Li, Q. Li, L. Xu, B. Zhang, J. Meng, Y. Wu and L. Mai, *Small*, 2017, **13**, 1701504.
- 33 H. Ejima, J. J. Richardson and F. Caruso, *Nano Today*, 2017, **12**, 136–148.
- 34 J. Guo, Y. Ping, H. Ejima, K. Alt, M. Meissner, J. J. Richardson, Y. Yan, K. Peter, D. von Elverfeldt, C. E. Hagemeyer and F. Caruso, *Angew. Chem., Int. Ed.*, 2014, **53**, 5546–5551.
- 35 H. Ejima, J. J. Richardson, K. Liang, J. P. Best, M. P. van Koevreden, G. K. Such, J. Cui and F. Caruso, *Science*, 2013, **341**, 154–157.
- 36 L. Yang, L. Han, J. Ren, H. Wei and L. Jia, *Colloids Surf., A*, 2015, **484**, 197–205.
- 37 M. A. Rahim, K. Kempe, M. Müllner, H. Ejima, Y. Ju, M. P. van Koevreden, T. Suma, J. A. Braunger, M. G. Leeming, B. F. Abrahams and F. Caruso, *Chem. Mater.*, 2015, **27**, 5825–5832.
- 38 X. W. Lou, Y. Wang, C. Yuan, J. Y. Lee and L. A. Archer, *Adv. Mater.*, 2006, **18**, 2325–2329.
- 39 Y. Lei, F. Qu and X. Wu, *Nano-Micro Lett.*, 2012, **4**, 45–51.
- 40 Z. Xiao, J. Meng, Q. Li, X. Wang, M. Huang, Z. Liu, C. Han and L. Mai, *Sci. Bull.*, 2018, **63**, 46–53.
- 41 X. Yu, J. Yu, B. Cheng and B. Huang, *Chem.–Eur. J.*, 2009, **15**, 6731–6739.
- 42 A. Krilov, A. Holmgren, R. Gref and L. O. Öhman, *Holzforschung*, 2009, **47**, 239–246.
- 43 Q. Zhang, Q. Gao, W. Qian, H. Zhang, Y. Tan, W. Tian, Z. Li and H. Xiao, *J. Mater. Chem. A*, 2017, **5**, 19136–19142.
- 44 Y. Zeng, J. Luo, Y. Wang, L. Qiao, B. Zou and W. Zheng, *Nanoscale*, 2017, **9**, 17576–17584.
- 45 S. Shilpa and A. Sharma, *J. Mater. Chem. A*, 2017, **5**, 14220–14229.
- 46 Y. Wang, Z. X. Huang, Y. Shi, J. I. Wong, M. Ding and H. Y. Yang, *Sci. Rep.*, 2015, **5**, 9164.